Multi-Photon Vertical Cross-Sectional Imaging With a Dynamically-Balanced Thin-Film PZT z-Axis Microactuator

Jongsoo Choi, Xiyu Duan, Haijun Li, Thomas D. Wang, and Kenn R. Oldham, *Member, IEEE*

***Abstract*— Use of a thin-film piezoelectric microactuator for axial scanning during multi-photon vertical cross-sectional imaging is described. The actuator uses thin-film lead-zirconate-titanate to generate the upward displacement of a central mirror platform micro-machined from a silicon-on-insulator wafer to dimensions compatible with endoscopic imaging instruments. Device modeling in this paper focuses on the existence of frequencies near device resonance producing vertical motion with minimal off-axis tilt, even in the presence of multiple vibration modes and non-uniformity in fabrication outcomes. Operation near rear resonance permits large stroke lengths at low voltages relative to other vertical microactuators. Highly uniform vertical motion of the mirror platform is a key requirement for vertical cross-sectional imaging in the remote scan architecture being used for multi-photon instrument prototyping. The stage is installed in a benchtop testbed in combination with an electrostatic mirror that performs in-plane scanning. Vertical sectional images are acquired from 15-μm diameter beads and excised mouse colon tissue. [2017-0073]**

***Index Terms*— Microelectromechanical systems, piezoelectric actuators, dynamics, biomedical imaging.**

I. Introduction

IN RECENT years, there have been many efforts to create endomicroscopy instruments with cellular or sub-cellular resolution and deep tissue penetration. Multi-photon microscopy offers both high resolution and significant imaging depth using intense ultrafast pulses of long wavelength light to excite shorter wavelength photons via nonlinear effects. Relative to other optical imaging modalities, multi-photon microscopy has benefits of reduced photobleaching and capacity to excite endogenous fluorescence, in addition to its compatibility with a variety of targeted fluorescent biomarkers.

Manuscript received March 29, 2017; accepted April 25, 2017. This work was supported in part by the National Science Foundation under Grant CMMI 1334340 and in part by the National Institutes of Health under Grant R01 EB020644. Subject Editor H. Jiang. *(Corresponding author: Jongsoo Choi.)*

J. Choi was with the University of Michigan, Ann Arbor, MI 48109 USA. He is now with Vesper Technologies Inc., Boston, MA 02110 USA (e-mail: jongs@umich.edu).

X. Duan and H. Li are with the Department of Internal Medicine, University of Michigan, Ann Arbor, MI 48109 USA.

T. D. Wang is with the Departments of Internal Medicine, Biomedical Engineering, and Mechanical Engineering, University of Michigan, Ann Arbor, MI 48109 USA.

K. R. Oldham is with the Department of Mechanical Engineering, University of Michigan, Ann Arbor, MI 48109 USA (e-mail: oldham@umich.edu).

Color versions of one or more of the figures in this paper are available online at http://ieeexplore.ieee.org.

Digital Object Identifier 10.1109/JMEMS.2017.2701798

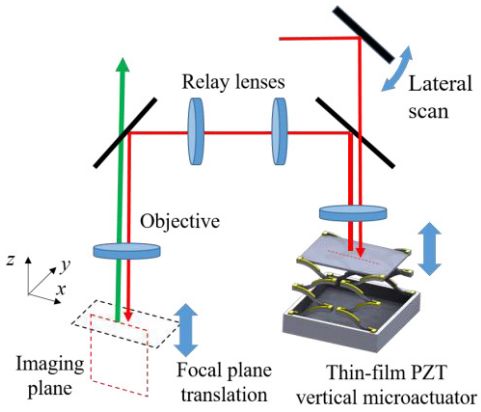

Fig. 1. Concept drawing of fast axial multi-photon image plane translation using a thin-film piezoelectric actuator in a remote scanning architecture.

To make best use of multi-photon imaging capabilities in a small instrument, it is desirable to support fast axial (also referred to as vertical or into-tissue) scanning of an ultrafast laser. Sufficiently fast axial scanning can support *in vivo* vertical optical sectioning, providing real-time cross-sectional images of tissue in the same plane that is used by histologists to diagnose and monitor diseases such as colon or esophageal cancer. However, previous endoscopic instruments have provided very limited support for altering depth-of-focus during multi-photon imaging. Several *en face* multi-photon endoscopes have characterized out-of-plane, or z-axis, resolution, but only by moving the sample being imaged [1], [2], [3]. Rivera *et al.* [4] provided a type of axial differentiation by imaging through three fibers offset over 130 μm, but without the possibility of further adjustment of imaging depth. Ouzanov *et al.* [5] and Bao *et al.* [6] designed instruments in which fiber position could be adjusted relative to distal optics, but this permitted only very slow focus adjustments.

Conceptually, fast z-axis scanning can be performed by microelectromechanical system (MEMS) actuators that support large out of plane displacements in very small chip sizes (Fig. 1). Large displacements in this context typically refers to translational motion on the order of 5% of total chip size or greater. The authors have previously reported thin-film lead-zirconate-titanate (PZT) piezoelectric actuators based on bend-up/bend-down piezoelectric beam designs by Qiu *et al.* [7] and Choi *et al.* [8], achieving up to 500 μm displacements with bandwidths on the order of 100-200 Hz. Other piezoelectric microactuators with large axial displacements

TABLE I
COMPARISON OF PERFORMANCE AMONG AXIAL SCANNING ACTUATOR TECHNOLOGIES

Actuator type	Dimensions (mm x mm x mm)	Axial Range (μm)	Z-axis Freq. (Hz)	Volts (V)	Power (mW)
Bulk piezoelectric (P-601.3S)	82 x 12 x 20	>400	290	120	~300
Electrostatic [14]	3.2 x 2.9 x 0.5	200-540	460	40-60	~2
Electrostatic [18]	1.5 x 1.5	1243	NR	273	NR
Electromagnetic [13]	3.2 x 3.2 x 0.5 (coil: 20 x 20 x 30)	>300	150-300	0-25	15
Electrothermal [12]	3 x 3 x ~0.5	800 (DC)	NR	6	~420
Thick-film PZT [11]	3 x 3 x ~0.5	42 (DC) 387 (AC)	930	±25	0.45
Thin-film PZT [9]	2 x 2 x 0.5	32	0-316	2	NR
Thin-film PZT [8] (quasi-static)	3.2 x 3.2 x 0.5	>500	0-120	0-20	<0.1
This Work: Thin-Film PZT (resonant)	**3 x 3 x 0.5**	**>200**	**116**	**0-4**	**<0.1**

include a thin-film piezoelectric tip-tilt design by Zhu *et al.* [9], though that actuator emphasized rotational scanning angle and thus had more limited scanning depth, and a bulk ceramic actuator with amplified motion by Domke *et al.* [10], though at a larger device size and high voltage. Aktakka *et al.* [11] demonstrated vertical piezoelectric actuation with planarized PZT films, though very large displacements were limited to relatively high frequency resonance. A number of electrothermal microactuators have also demonstrated large vertical displacements [12], but these can be limited in speed by thermal time constants. Electromagnetic microactuators achieving comparable displacements have required sufficiently large driving coils to increase instrument size or impede field-of-view [13]. Electrostatic microactuators have also achieved large vertical displacements at similar chip sizes using parametric resonance [14], [15], though high voltages and generally high operating frequencies are required. A summary of representative micro-scale vertical scanning imaging technologies is provided in Table 1.

This work adapts previous thin-film piezoelectric vertical actuation for rapid adjustment of multi-photon imaging depth, and demonstrates the first use of a thin-film piezoelectric actuator for vertical multi-photon cross-sectional imaging of tissue. Relative to prior actuators, as seen in Table I, thin-film piezoelectric actuation has two primary advantages: (1) at resonance, the focus of this work, larger vertical displacements can be achieved at lower voltage and power than by other transduction mechanisms; (2) the possibility to switch between resonant and quasi-static operation provides potential long-term possibilities for switching between fast vertical cross-sectional scanning modes and lateral cross-sectional scanning, or to perform mechanical zoom or laser interrogation/micro-surgery type tasks.

The paper is organized as follows: Section II introduces the remote-scan multi-photon imaging architecture and associated actuator specifications. Section III summarizes the actuator design and analyzes vertical versus off-axis dynamic motion of closely-spaced modes during near-resonance operation of such an actuator based on compliant deformation of elastic beams about a central mirror platform. Section IV describes the fabrication process for the actuators, and Section V provides experimental actuation and imaging results. Section VI discusses implications of actuator performance, and concludes the paper.

II. MULTI-PHOTON IMAGING AND ACTUATOR REQUIREMENTS

In multi-photon imaging, fluorescence at a given wavelength is excited by multiple lower-energy, longer wavelength photons delivered by a high-power, ultra-fast laser. Excitation of fluorescence nonlinearly with photon intensity is beneficial for reducing light received from laser scattering in biological tissue and reducing associated photobleaching, while use of relatively long wavelength excitation permits significant imaging depths. Taken together, this makes multi-photon imaging a desirable technique for imaging beneath the tissue surface in hollow organs, with potential to produce vertical cross-sectional images of tissue, providing minimally invasive imaging in the same vertical planes commonly used by histologists to diagnose and monitor disease.

To generate vertical cross-sectional images, it becomes necessary to actively scan the focal plane of a multi-photon laser rapidly through the depth of tissue to be imaged. This requires a scanning mirror that can translate axially, or perpendicular to the tissue surface, in a compact instrument size. In this work, axial translation of a scanning mirror is relayed to the objective of an imaging system in a remote scan architecture after Botcherby *et al.* [16] and Duan *et al.* [17]. While the imaging system is implemented in this paper as a benchtop prototype, for small animal and/or clinical applications such an architecture is ideally implemented in a handheld form factor or ultimately fully endoscope-compatible form factor. A representative handheld form factor has been previously demonstrated for multi-photon imaging in the lateral plane with 3.4 mm diameter distal optics and scanning assembly approximately 2 cm in width [23], while endoscope compatibility requires a total instrument diameter of 5.5 mm or smaller to function in

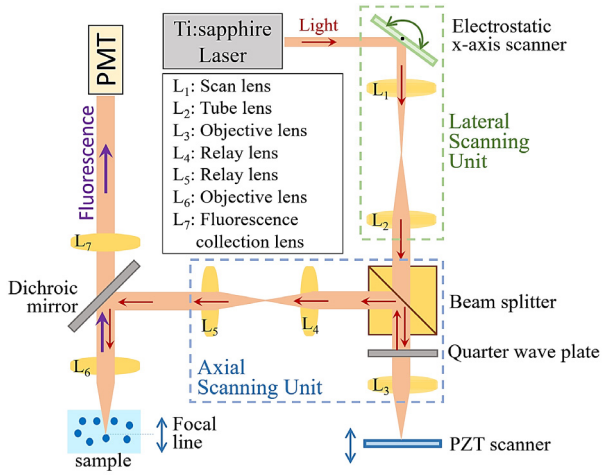

Fig. 2. Schematic of multi-photon vertical cross-sectional imaging system.

commercially available endoscope instrument channels. This targeted instrument miniaturization thus makes MEMS-based axial mirror scanning highly-desirable for multi-photon vertical sectioning.

The testbed used in this work is shown schematically in Fig. 2. It is based on a Ti-Sapphire laser (Mai Tai DeepSee HP DS) that is first directed onto an electrostatic rotational scanning mirror. This mirror provides fast lateral scanning in the x-and/or y- axis via parametric resonances with operating frequency near 9.4 kHz or 2.0 kHz for the respective axes. Details of electrostatic lateral scanner design have been reported in [17]. The beam is expanded by a pair of lenses, L_3 (f = 25 mm, LA1951-B, Thorlabs) and L_4 (f = 100 mm, LA1509-B, Thorlabs) to match the back aperture of an aspheric focusing lens (L_3, C230TMD-B, Thorlabs). In this process, the beam is passed through a beam splitter (polarizing, PBS252, Thorlabs) and a quarter wave plate (WPQ10M-780, Thorlabs). This allows the beam to be directed towards the objective after reflecting off the PZT scanner. After passing through a pair of relay lenses, L_4 and L_5 (both f = 75 mm, LA1608-B, Thorlabs), a dichroic mirror (650DCSPSR) directs the beam to the back aperture of the objective, L_6 (LUMPlanFL/IR 60x/0.9w, NA = 1, Olympus).

Fluorescence returning from the sample passes back through the objective and dichroic mirror to the detector. It is focused by lens L_7 (f = 50 mm, LA11134-A, Thorlabs) onto a photomultiplier tube, or PMT (H7422-40, Hamamatus). The PMT signal was amplified by a high current amplifier (59-178, Edmund Optics) and collected by a high-speed data acquisition board (National Instruments, PCI-6115).

To acquire vertical cross-sectional images from this imaging system, the electrostatic lateral scanning mirror is operated in single lateral scan axis while the PZT scanner translates in the z-axis or axial direction. As the PZT scanner moves above or below the focal point of L_3, the wavefront of the beam diverges or converges after reflection by the polarized beam splitter. This causes the focal point of the beam after the objective, L_6, to be translated approximately proportionally in the sample being imaged.

TABLE II
ACTUATOR SPECIFICATIONS FOR EVENTUAL HANDHELD/ ENDOMICROSCOPIC MULTI-PHOTON IMAGING IN A REMOTE SCAN, VERTICAL SECTIONING CONFIGURATION

Specification	Units	Target
Max. Areal Dimension /	mm x mm /	< 3.4 x 3.4
Diameter	mm	/ 5.0
Axial displacement	µm	> 200
Scanning speed	Hz	> 10
Non-uniformity	°	< 0.5

While instrument sizes constrain MEMS scanner dimensions, imaging requirements and optical design dictate other performance specifications. Prior multi-photon endomicroscopes imaging in the lateral plane at varying depths by either moving a tissue sample [2], [3] or adjusting their optical position [5], [6] have demonstrated imaging depths ranging from 30-250 μm, and a target imaging depth of 200 μm was selected for this work based on those results and some additional experiments on imaging quality versus depth [24]. The exact relationship between axial mirror translation and focal depth translation depends on lens selection, but for the remote scan design implemented here, magnification ratio is approximately 2:1. For a target actuator displacement of 200 μm, this would potentially permit imaging of the entire cross-section of the epithelium of a mouse colon, up to about 400 μm in depth. Minimum actuator bandwidth was also selected to be 10 Hz for adequate imaging rate and avoidance of motion aberrations, though in practice this is not a limiting constraint given small actuator size and thus much higher resonant frequencies.

Instead, the stricter constraint on actuator performance and primary subject of analysis in this paper is actuator uniformity. Because the axial scanning mirror is located a significant distance from the distal optics, off-axis motion of the mirror (i.e. tilt) as it translates can cause significant degradation of image quality. For example, in the prototype system, off-axis tilt of 1.6° was calculated by optical simulation to reduce laser intensity by over 20%, implying even greater loss of fluorescence given nonlinear multi-photon effects. The piezoelectric scanning mirrors discussed here were selected to be targeted for operation with less than 0.5° tilt over their 200 μm range of motion. Specifications for actuator performance as discussed above are summarized in Table II.

It is worth noting that thin-film piezoelectric actuators are not the only technology for which remote scanning actuator requirements might be achieved. Electrostatic and thick-film piezoelectric vertical actuators can achieve sufficient displacement if substantially higher scanning frequencies remain compatible with sufficient light collection, and in fact one such electrostatic device has been tested in multi-photon imaging previously [17]. Electrothermal microactuators have demonstrated sufficient range and uniformity, suitable for implementation if much larger heat dissipation and thermal time constants can be accommodated. The thin-film piezoelectric actuators evaluated in this work lie in an intermediate range of range of motion and operating speed, with practical advantages

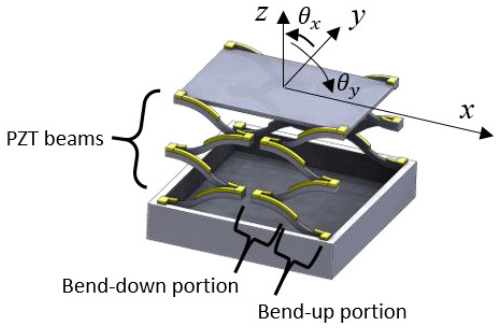

Fig. 3. Schematic diagram of proposed piezoelectric microactuator deformation under nominal conditions is generated by a combination of bend-up and bend-down bending deformations structured sequentially through four piezoelectric serpentine legs surrounding the central mirror platform (not drawn to scale).

from reduced voltage and power requirements, and potential performance benefits from possible future use moving between resonant and quasi-static operation modes.

III. Actuator Design and Dynamics

After a brief discussion of device design, the modeling focus of this paper is on achieving strict uniformity of MEMS actuator displacement, i.e. nearly single axis motion, which can be difficult to achieve due to both non-idealities of actuator fabrication and the presence of multiple vibration modes in compliant elastic structures. There are various candidate methods for compensating for non-uniformity of actuator motion. One method is through calibration of the actuator model [8] and associated voltage gains at individual legs of an actuator to achieve uniform quasi-static displacements. This approach, however, increases instrument complexity due to additional interconnect requirements to the scanning actuator. Another approach is to implement a feedback control system [25], though again with an associated increase in system complexity of applying multiple inputs and acquiring on-chip sensor data. The approach taken in this work is to identify desirable frequencies for resonant operation where superposition of modes produces uniform z-axis motion, though this may not occur at the peak resonant frequency and may lack guarantees of robustness. Dynamic analysis in the following section evaluates under what conditions a desired level of uniformity can be reliably achieved for a nominally symmetric vertical stage experiencing resonance in multiple axes.

A. Dynamic Model for Off-Axis Motion

The basic structure of the thin-film piezoelectric microactuator used for multi-photon imaging is shown in Fig. 3. A central mirror or mirror platform is supported by four serpentine piezoelectric bending legs, with piezoelectric stack materials varied to produce selective bend-up or bend-down motion in successive segments of the beams.

The bend-up, bend-down architecture is generated by manipulating the position of the neutral axis of the legs relative to midline of the PZT thin-film using a structural metal layer applied periodically over the serpentine structures. In its nominal design, this bend-up, bend-down arrangement limits the out-of-plane bending moment generated at the tips of individual legs, and with proper film thickness and ratios of bend-up to end-down lengths, can enhance vertical range of motion compared to use of a single bending direction throughout the legs. Analysis of static leg bending displacement, across single [7] and multiple [8] axes has been previously reported. In practice, the actuator's legs are also deformed by residual stresses generated during the fabrication process. If bending due to residual stress is modest (i.e., consistent with small angle approximations during beam bending, or $\sin(\theta) \approx \theta$), leg deformation becomes the superposition of the static deformation due to residual stress and the time varying displacement of the stage due to the additional bend-up, bend-down deformation induced by an applied voltage.

While linear, single-axis dynamics of this type of thin-film PZT vertical scanning actuator have been studied in the works noted above ([7], [8]), the strict uniformity requirements of the proposed remote scanning multi-photon imaging system requires further analysis of non-ideal and off-axis dynamic effects. In its linear dynamic regime, the scanner can be modeled as a mass-spring-damper system,

$$\mathbf{M}\ddot{\mathbf{x}} + \mathbf{C}\dot{\mathbf{x}} + \mathbf{K}\mathbf{x} = \mathbf{B}u \tag{1}$$

where the relevant states of the system are z-axis translation, z, and rotations about the x- and y- axes as defined in Fig. 2, θ_x and θ_y, collected in state vector $x = [z\theta_x\ \theta_y]^T$, $\mathbf{M}$ and $\mathbf{C}$ are equivalent inertia and damping matrices for the respective axes, $\mathbf{K}$ is the net effective stiffness matrix from the four legs as connected to the central mirror platform, and input matrix $\mathbf{B}$ contains gain information from the applied voltage, u, to net forces and moments applied to the mirror platform.

The total stiffness and input matrices are the summation of contributions from the individual legs,

$$\mathbf{K} = \sum_{\mathbf{i=1}}^{\mathbf{4}} \mathbf{T}_i\mathbf{K}_i\mathbf{S}_i \tag{2}$$

$$\mathbf{B} = \sum_{\mathbf{i=1}}^{\mathbf{4}} \mathbf{T}_i\mathbf{B}_i \tag{3}$$

where $\mathbf{K_i}$ and $\mathbf{B_i}$ are the multi-axis stiffness and forcing from leg i, T_i is the matrix converting forces and moments at the tip of the i-th leg to the forces and moments felt at the platform center of mass, and $\mathbf{S_i}$ is the matrix converting translation and rotation of the platform to three-axis displacement of the platform at the tip of the i-th leg.

Under ideal, perfectly symmetric conditions with identical actuation legs, there is no net moment generated by the combined forcing from (3) or cross-axis stiffness terms in (2), and the dynamics from (1) become decoupled into individual axes, with net input force due to voltage only in the vertical z-direction. In practice, slight variation in dimensions or piezoelectric coefficient across the legs results in perturbations to the nominal system model, leading to coupling between axes and deviation of stage motion from a uniform vertical displacement. To analyze this behavior, the remainder of this section focuses on dynamic coupling effects, while a summary of individual leg modeling and forcing is provided in Appendix A, with resulting parameters summarized in Table 3.

TABLE III
NOMINAL ACTUATOR MODEL PARAMETERS

Parameter	Units	Nominal value
Effective mass (m)	mg	.17
Effective y-axis inertia (J_y)	mg-mm^2	0.79
Net z-axis stiffness (k_{zz})	mN/m	0.09
Net y-axis stiffness ($k_{\theta\theta}$)	mN-mm/rad	0.44
Leg cross-axis stiffness ($k_{z\theta}$, $k_{\theta z}$)	mN/rad	-0.05
Damping ratios (ξ_z, ξ_θ)		0.05
Net z-axis gain (b_z)	μN/V	4
Leg cross-axis gain (b_θ)	μN-mm/V	1.2

In the PZT scanner, coupling effects are most significant for closely-spaced vibration modes, which arise from the primary z- and θ_y- (rotation about the long axis of the mirror) axes of the scanner at its current dimensions. The reduced order dynamics of the system (state vector $\mathbf{x}_r = [z\ \theta_y]^T$) can be summarized in the form

$$\begin{bmatrix} m & 0 \\ 0 & J_y \end{bmatrix}\ddot{\mathbf{x}}_r + \begin{bmatrix} c_z & 0 \\ 0 & c_\theta \end{bmatrix}\dot{\mathbf{x}}_r + \begin{bmatrix} k_{zz}+\delta_{zz}k_{zz} & \delta_{z\theta}k_{z\theta} \\ \delta_{\theta z}k_{\theta z} & k_{\theta\theta}+\delta_{\theta\theta}k_{\theta\theta} \end{bmatrix}\mathbf{x} = \begin{bmatrix} b_z+\delta_{bz}b_z \\ \delta_{b\theta}b_\theta \end{bmatrix}u \tag{4}$$

where m is mass of the equivalent mass of the central platform and legs; J_y is equivalent rotational inertia of the central platform and legs; c_z and c_θ are damping constants in the two axes; δ_{zz} and $\delta_{\theta\theta}$ are the proportional deviation of the net z-axis and θ_y axis stiffnesses from their nominal values, k_{zz} and $k_{\theta\theta}$; δ_{bz} is the proportional deviation of the net input forcing in the z-axis, b_z; $\delta_{\theta z}$ and $\delta_{z\theta}$ describe the net cross-axis stiffness due to asymmetries in the proportional to the cross-axis stiffnesses of the individual legs, $k_{\theta z}$ and $k_{z\theta}$; and $\delta_{b\theta}$ describes the net bending moment due to asymmetries in the proportional to the bending moment generated by a nominal individual leg, b_θ.

Multiplying through (4) by the inverse of the mass matrix, the system can be cast in terms of natural frequencies and damping ratios as

$$\ddot{\mathbf{x}}_r + \begin{bmatrix} 2\xi_z\omega_z & 0 \\ 0 & 2\xi_\theta\omega_\theta \end{bmatrix}\dot{\mathbf{x}}_r + \begin{bmatrix} \omega_z^2+\delta_{zz}\omega_z^2 & \delta_{z\theta}\frac{k_{z\theta}}{k_{zz}}\omega_z^2 \\ \delta_{\theta z}\frac{k_{\theta z}}{k_{\theta\theta}}\omega_\theta^2 & \omega_\theta^2+\delta_{\theta\theta}\omega_\theta^2 \end{bmatrix}\mathbf{x} = \begin{bmatrix} \frac{b_z}{m}+\delta_{bz}\frac{b_z}{m} \\ \delta_{b\theta}\frac{b_\theta}{J} \end{bmatrix}u \tag{5}$$

where ω_z and ω_θ are the nominal natural frequencies of the modes being examined, and ξ_z and ξ_θ are their damping ratios. This can be summarized in the form

$$s^2\mathbf{X}(s) + s\Gamma\mathbf{X}(s) + \Lambda\mathbf{X}(s) = \beta U(s) \tag{6}$$

where s is the Laplace operator, Γ is the damping coefficient matrix, Λ is the natural frequency matrix, and β is the normalized input matrix.

The transfer functions for the system from input u to output z and θ_y can be computed from standard Laplace transform analysis,

$$\begin{bmatrix} \frac{Z(s)}{U(s)} \\ \frac{\Theta(s)}{U(s)} \end{bmatrix} = \left(s^2+s\Gamma+\Lambda\right)^{-1}\beta \tag{7}$$

To give:

$$\begin{bmatrix} \frac{Z(s)}{U(s)} \\ \frac{\Theta(s)}{U(s)} \end{bmatrix} = \begin{bmatrix} \frac{\left(s^2+2\xi_\theta\omega_\theta s+\omega_\theta^2+\delta_{\theta\theta}\omega_\theta^2\right)\left(\frac{b_z}{m}+\delta_{bz}\frac{b_z}{m}\right)+\left(-\delta_{z\theta}\frac{k_{z\theta}}{k_{zz}}\omega_z^2\right)\delta_{b\theta}\frac{b_\theta}{J}}{\det(s^2+s\Gamma+\Lambda)} \\ \frac{\left(\delta_{\theta z}\frac{k_{\theta z}}{k_{\theta\theta}}\omega_\theta^2\right)\left(\frac{b_z}{m}+\delta_{bz}\frac{b_z}{m}\right)+\left(s^2+2\xi_z\omega_z s+\omega_z^2+\delta_{zz}\omega_z^2\right)\delta_{b\theta}\frac{b_\theta}{J}}{\det(s^2+s\Gamma+\Lambda)} \end{bmatrix} \tag{8}$$

To be able to achieve a specified vertical displacement, z_{min}, with a sufficiently small off-axis tilt, θ_{max}, it is necessary that at some frequency the respective gains of the system satisfy

$$\left|\frac{Z(j\omega)}{U(j\omega)}\right|u_{pp} > z_{min}, \left|\frac{\Theta(j\omega)}{U(j\omega)}\right|u_{pp} < \theta_{max} \tag{9}$$

where ω is the operating frequency and u_{pp} is the peak-to-peak amplitude of a sinusoidal input voltage.

This can be reduced to a worst case analysis as a function of the maximum perturbation to individual model elements, Δ, i.e. $\delta < \Delta$ for all δ terms with their respective subscripts appearing in (8). Specifically, treating certain higher-order perturbation terms in (8) as negligible (i.e. $\delta_{z\theta}\ \delta_{b\theta} \approx 0$, etc.) which is a close approximation if $\Delta << 1$, the frequency having the maximum worst gain ratio between desired z-axis motion and undesired tilt is required to satisfy:

$$\max_{\omega}\min_{\delta_{**}<\Delta}\left|\frac{\left(-\omega^2+2\xi_\theta\omega_\theta\omega j+\omega_\theta^2+\delta_{\theta\theta}\omega_\theta^2\right)\left(\frac{b_z}{m}+\delta_{bz}\frac{b_z}{m}\right)}{\left(-\omega^2+2\xi_z\omega_z\omega j+\omega_z^2+\delta_{zz}\omega_z^2\right)\delta_{b\theta}\frac{b_\theta}{J}+\left(\delta_{\theta z}\frac{k_{\theta z}}{k_{\theta\theta}}\omega_\theta^2\right)\frac{b_z}{m}}\right| > \frac{z_{min}}{\theta_{max}} \tag{10}$$

where δ_{**} refers to minimization over all remaining δ terms. This optimization can be solved piece-wise analytically or numerically to provide a bound on permissible maximum perturbation of actuator dynamics parameters meeting a specified level of uniformity.

B. Dynamic Analysis Results

Based on the discussion above, candidate properties of a vertical scanning actuator that influence its off-axis or tilting amplitude damping ratios, natural frequency ratio ω_θ/ω_z, relative cross axis stiffnesses of the system, $k_{z\theta}/k_{zz}$ and $k_{\theta z}/k_{\theta\theta}$, and relative strength of possible off-axis forcing, $(b_z/m)/(b_\theta/J)$. Fig. 4 shows a sample relationships between the bound on individual parameter uncertainty, Δ, for an actuator and its worst-case gain ratio at its best candidate operating frequency. Various frequency ratios between its z-axis and θ_y-axis modes are shown; other nominal parameters are from the piezoelectric scanner design to be tested ($k_{z\theta}/k_{zz} = -0.55$ mm, $k_{\theta z}/k_{\theta\theta} = -110\ m^{-1}$, $(b_z/m)/(b_\theta/J_y) = .015$ m/rad, $\xi_z = \xi_\theta = 0.05$). Also shown is the ratio

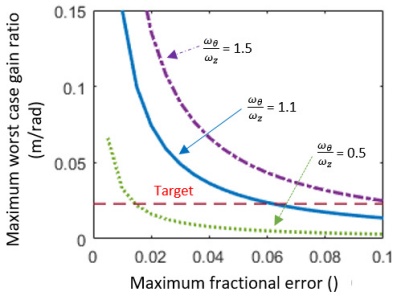

Fig. 4. Worst case z-axis to θ_y-axis gain for PZT scanner for various nominal resonance frequency ratios ($k_{z\theta}/k_{zz} = -0.5$ mm, $k_{\theta z}/k_{\theta\theta} = -100\ m^{-1}$, $(b_z/m)/(b_\theta/J) = 0.015$ m/rad, $\xi_z = \xi_\theta = 0.05$).

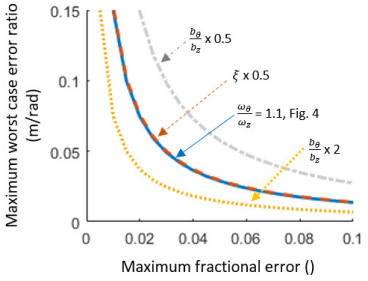

Fig. 5. Worst case z-axis to θ_y-axis gain for PZT scanner under other example nominal operating parameters, showing limited sensitivity to damping and cross-axis stiffness variation, but substantial sensitivity to off axis forcing (if not otherwise scaleded, $\omega_\theta/\omega_z = 1.1$, ($k_{z\theta}/k_{zz} = -0.5$ mm, $k_{\theta z}/k_{\theta\theta} = -100\ m^{-1}$, $(b_z/m)/(b_\theta/J) = 0.015$ m/rad, $\xi_z = \xi_\theta = 0.05$).

of 200 μm to 0.5° targeted for operating the PZT scanner in the remote scanning testbed, or 0.023 m/rad. As can be seen, lower relative frequencies for the off-axis mode result in stricter requirements on actuator uniformity to avoid excessive off-axis motion. Even when frequencies are very closely spaced, say within 10%, some operating regions are predicted to exist where high quality z-axis displacement can be maintained.

Fig. 5 examines some other hypothetical scenarios for PZT scanner design and operation, when $\omega_\theta/\omega_z = 1.1$. The relative strength of possible off axis forcing, b_z/b_θ, can be seen to be the most significant influence on parameter error tolerance for a given actuator mass and inertia. Changes in damping ratio and cross-axis spring constants causing very little change from the original scenario. The limited effect of damping is taken to be the case when damping ratios are relatively consistent across modes. Cross-axis spring constants have limited effects because a much larger contribution to stiffness coupling across axes is the contribution of individual spring stiffnesses in the k_{zz} direction acting on the moment arms from the mirror platform center to the leg connection points.

While analysis in Section III.A. and resulting bounds from (10) are convenient for rapidly assessing design robustness, such analysis can both overstate and understate the difficulty of selecting a frequency at which uniform vertical motion of this class of actuators can be achieved. On one hand, bounds from (10) are based on the worst-case accumulation of perturbations to individual model parameters and, in effect, individual leg properties underlying those parameters. Thus, a substantial number of perturbed systems may still meet

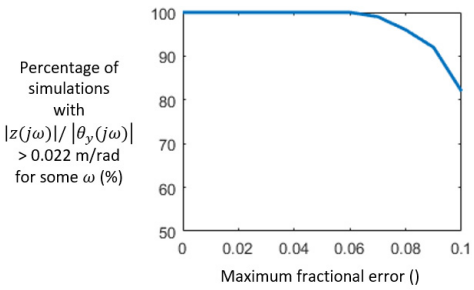

Fig. 6. Simulation of randomly perturbed full-order dynamics at nominal design parameters ($k_{z\theta}/k_{zz} = -0.008$ m, $k_{\theta z}/k_{\theta\theta} = -100\ m^{-1}$, $(b_z/m)/(b_\theta/J) = 750$ rad/m, $\xi_z = \xi_\theta = 0.05$) shows that first failure of any operating frequency to achieve desired motion occurs at $\Delta = 0.07$, exactly in agreement with the reduced order bound, and with a large percentage of random systems continuing to meet specification after performance is no longer guaranteed.

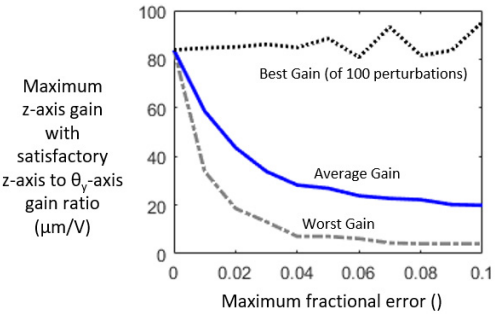

Fig. 7. Although simulated systems from Fig. 6 can achieve target translational to tilt dynamic gains, typical z-axis gains meeting motion requirement drop substantially, implying that larger voltages may be needed to meet specified z-axis displacements.

uniformity requirements even when the worst-case analysis for parameter perturbations is violated. On the other hand, (10) does not address the specific gain at which a system achieves sufficient uniformity, which many result in substantially higher voltage requirements than would be necessary for the nominal system.

To assess the importance of these effects, a set of sample systems with nominal PZT scanner design parameters and $\omega_\theta/\omega_z = 1.1$ was simulated over 100 randomly distributed perturbations at various maximum perturbation levels, Δ. Fig. 6 shows the percentage of simulated system at each perturbation level that passed the uniformity requirement at some frequency, while Fig. 7 shows the minimum, mean, and maximum gains of the system in the z-axis directions at each perturbation level. Simulations in these tests were performed using the full, 3-axis, system model, not just two-mode reduced order model used for analytical robustness analysis.

As can be seen in Fig. 6, the first failures of the perturbed full-order system model to contain an operating frequency achieving the desired gain ratio occur around 7% parameter error, identical to the prediction of the bounds calculated from (10) shown previously in Fig. 4. Even above that ratio, large percentages of actuators would be expected to be capable of pure z-axis translation, still above 80% yield up to 10% parameter variation. On the other hand, the maximum

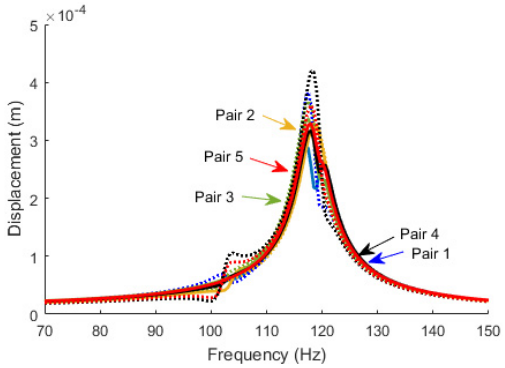

Fig. 8. Representative examples of randomly perturbed simulated system frequency response for δ's $< \Delta = 0.05$, with amplitude at mirror center (solid lines)and right edge (dotted lines) shown for each simulated case. Arrows mark maximum displacement for a 4 Vpp input where sufficiently small off-axis tilting would be obtained, for comparison to imaging tests.

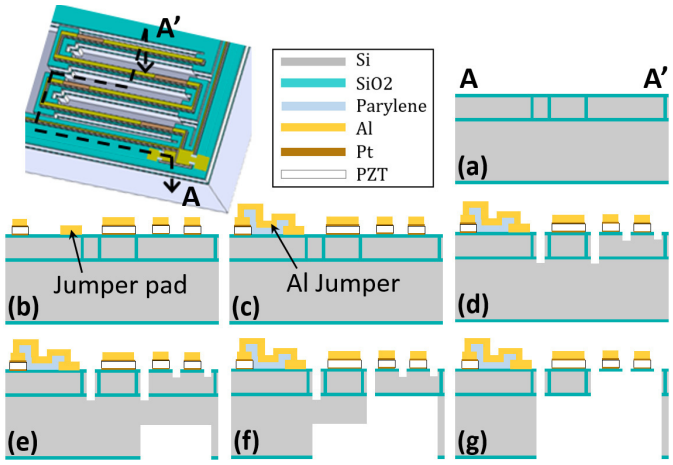

Fig. 9. Fabrication process (not drawn to scale): (a) silicon dioxide refilled trench; (b) deposition of thin-film PZT and metal stack; (c) formation of Al jumpers; (d) two-step top side DRIE; (e) initial backside DRIE; (f) full-area backside DRIE; (g) DRIE etching of device silicon layer.

z-axis gains where translational to tilt displacement is satisfactory decreases rapidly with parameter error. By about 2% error, up to 10 V may be necessary to guarantee that any given scanner can achieve 200 μm displacements, and at the 7% limit this becomes true of even the average scanner. For a sense of how this device variation manifests itself, Fig. 8 shows the first 5 simulated frequency response curves at a 3% perturbation limit when driven by a 4 Vpp sine wave, with response at both the center and right edge of the mirror platform shown. Locations where highest gains with sufficient uniformity are labeled, i.e. where mirror edge displacement is within about 10 μm of the mirror for less than 0.5° tilt at maximum displacement.

IV. Actuator Fabrication

Actuators are fabricated by the process shown in Fig. 9, starting with a silicon-on-insulator wafer with 30 μm device layer and 0.5 μm buried oxide. First, narrow (3 μm) trenches are etched by deep reactive-ion etching (DRIE) to the buried oxide layer, and refilled by tetraethyl orthosilicate (TEOS) chemical vapor deposition (CVD) silicon dioxide (Fig. 9a). The top surface of the wafer is chemically-mechanically polished and coated with an additional high temperature low pressure chemical vapor deposited (LPCVD, 0.5 μm) silicon dioxide that provides a uniform base layer for PZT deposition. The isolated structures in the device layer produced by this step become precisely defined rigid silicon elements of the completed platform, such as the frame and mirror platform.

Bottom electrode (Ti/Pt, 200 nm, unannealed), piezoelectric (PNZT seed/chemical solution PZT, 1.2 μm) and top electrode (Pt, 120 nm) are next deposited on the prepared wafer. The PZT thin-film is a 52/48 composition by Radiant Technologies, Albuquerque, NM, with typical reported sintering temperature of 650° C and maximum processing temperature 850° C [26], [27]). Top platinum, the PZT layer, and bottom platinum are sequentially patterned by reactive-ion etching (RIE). A structural aluminum layer (1 μm) is then patterned by a lift-off process to the top surface of select regions of the electrodes, to improve bond-pad strength and adjust the neutral axis of bend-down portions of cantilever beams (Fig. 9b). To further improve reliability of electrical interconnects, a chemical vapor deposition parylene-C film (560 nm), PECVD silicon dioxide (230 nm) layer, and additional aluminum layer (1 μm) are deposited to create electrical jumpers from the top and bottom electrodes of the PZT film to bond pads patterned directly on the silicon dioxide wafer surface, which were found to have much better reliability for wire bonding necessary in the confined space of endomicroscopy instruments (Fig. 9c).

Release of actuators from the silicon wafer was performed using a series of deep trench etching steps. First, silicon DRIE and silicon dioxide RIE steps were performed to etch through the buried oxide between actuation legs (Fig. 9d). Then, two-level backside DRIE is performed, with initial etching beneath the actuation legs (Fig. 9e), then full backside area etching beneath all moving parts (Fig. 9f). By etching the silicon dioxide layer exposed initially by the deeper portion of the backside etch before completing the backside DRIE process, free-standing thin-film PZT beam elements could be released, while retaining a solid silicon platform as a mirror platform or as the mirror itself (Fig. 9g). During this last release step, non-uniform etching of silicon or the formation of micro-columns or grass can be handled with SF_6 or XeF_2 etching thanks to the silicon-dioxide-filled trenches formed in the earlier step (Fig. 3a). With optimized etching parameters and layer thicknesses, the formation of the protective silicon dioxide trenches in the device layer (Fig. 9a) can be omitted.

V. Experimental Results

A. Actuator Testing

Examples of completed piezoelectric vertical actuators are show in Fig. 10, both before and after installation in a 3D-printed fixture for assembly to the imaging system. Stage displacement after fabrication was initially performed using a Keyence Profiler LJ-V7001P. The prototype actuators show about 300 μm static z-axis displacement at 14V_{DC}. As anticipated in the proceeding sections, some vertical displacement

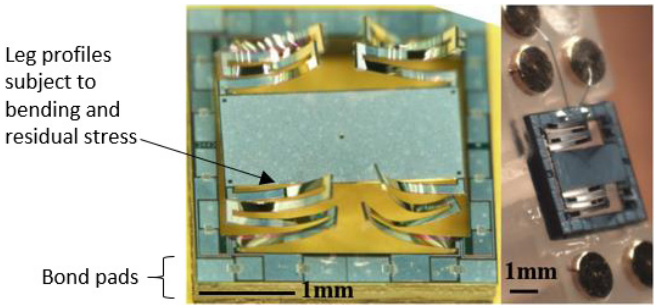

Fig. 10. Optical images of prototype microactuators before (left) and after (right) installed in a fixture.

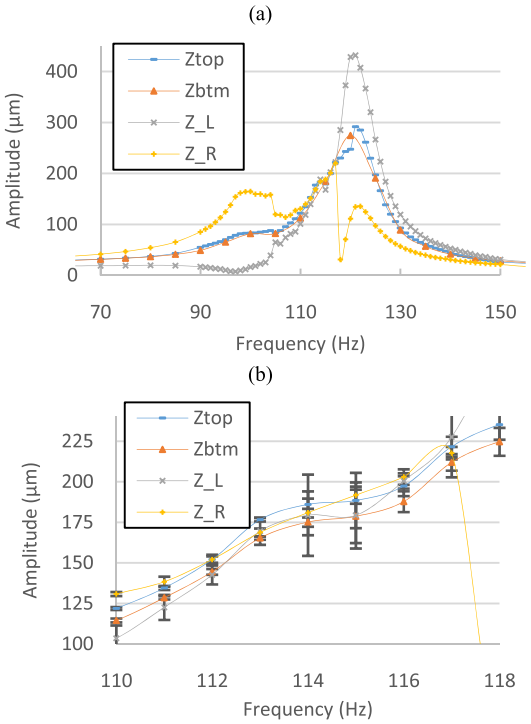

Fig. 11. Frequency sweep with $4V_{pp}$ $2V_{off}$ sinusoidal input over (a) 70-150 Hz and (b) in detail at 110-118 Hz, where maximum pure z-rotation was found to occur. Displacements at top (Ztop), bottom (Zbtm), left (Z_L), and right edges (Z_R) of the central mirror platform shown.

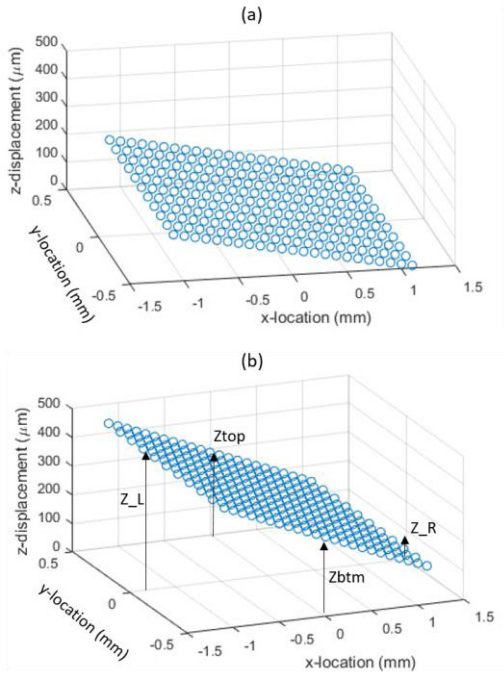

Fig. 12. Stage positions at maximum displacement at (a) 95 Hz and (b) 120 Hz resonances; laser measurement points labeled in (b).

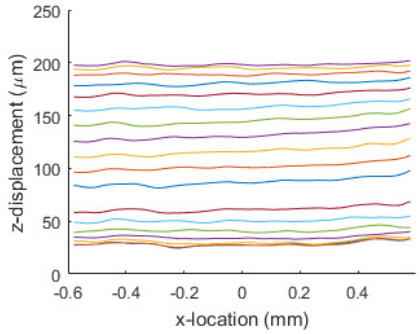

Fig. 13. Snapshots of stage x-z profile at various times during one cycle of steady-state motion under 114 Hz, 4 Vpp, 2 V offset sinusoidal actuation cycle show worst discrepancy between left and right mirror edges of approximately 8 μm.

is sacrificed in due to the asymmetry and residual stress on bending legs that was developed from the fabrication process and observed to cause the legs to generate twisting motion, rather than pure vertical. These non-idealities also prevented a pure vertical motion of the stage with a single input, resulting in 5.3° and 6.6° of tilting in the θ and φ directions, respectively. Dynamic response was evaluated using a swept sine input at lower voltages, and confirmed that first dynamic modes associated with z-axis displacement and rotation about the x- and y-axes were present in the range of approximately 90-150 Hz, as shown in Fig. 11a. Deviations from pure z-axis motion take the form of resonant peaks with coupled translation/tilt displacement above and below the frequency at which pure z-axis translation would have been anticipated, a situation commonly seen in simulated scenarios such as those shown in Fig. 8.

Fig. 11(b) shows detailed displacement amplitudes across the mirror in the range of 110-118 Hz, where best pure-z translation was found to occur. Optimal scanning at frequencies modestly below the peak resonance is also common in simulated scenarios, again as in Fig. 8. Error bars in Fig. 11(b) are generated from repeated tests of the actuator, to assess actuator stability at the frequencies to be used in imaging. To provide a sense of the contrast between individual resonance modes and dynamically-balanced frequencies, Fig. 12 shows the maximum displacement profiles of the stage at 95 Hz and 120 Hz, while Fig. 13 shows stage height evolution over time at 114 Hz, after compensating for any static off-axis tilt due to residual stress. It can be seen that both modes in Fig. 12 consist of a mix of z-axis translation and stage tilt about the y-axis, while at the balanced frequency, high-quality vertical motion can be achieved.

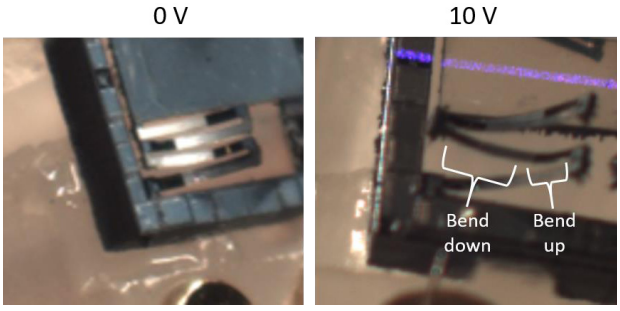

Fig. 14. In completed devices, bend-up and bend-down behavior of the PZT actuation layer acts in superposition on initial curvature of beams due to residual stress. Static deformation at 0 and 10 V shown.

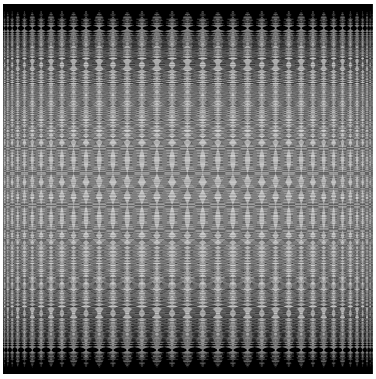

Fig. 15. RepresentativeLissajous scan patterned created by combined electrostatic lateral (9300/2 Hz) and piezoelectric vertical scanning (114 Hz), with trajectory generated in Matlab.

Snapshots of individual static leg deformations are shown in Fig. 14. Although the leg has a permanent initial curvature due to residual stress, additional bend-up and bend-down internal moments from the PZT result in comparatively more- and less-curved segments of the legs. The resulting accumulated change in height across the four segments of each leg produces the net displacement of the central platform, in superposition over the original static deformation.

B. Imaging

PZT actuator installation was begun by assembling the piezoelectric actuator to a mounting fixture, with the actuator manually positioned to eliminate any static off-axis tilt of the scanning mirror. The mirror was then placed before the axial scan objective, L_3, and uniformity of vertical scanning motion was verified. A Lissajous scan pattern combining piezoelectric axial scanning at 114 Hz and electrostatic lateral scanning at $60V_{pp}$ 9372 Hz was then initiated using Labview control software, as shown in Fig. 15. Imaging was performed at an input laser power of 20 mW and frame rate of 1 Hz during benchtop testing.

Sample images acquired in vertical sectioning mode are shown in Fig. 16. Fig. 16(a) shows several 15 μm diameter beads coated with fluorescein dye (FITC) in a polydimethylsiloxane polymer matrix, used as a simple tissue phantom for basic imaging system evaluation. Fig. 16(b) shows a cross-section of excised mouse colon epithelial tissue; this tissue

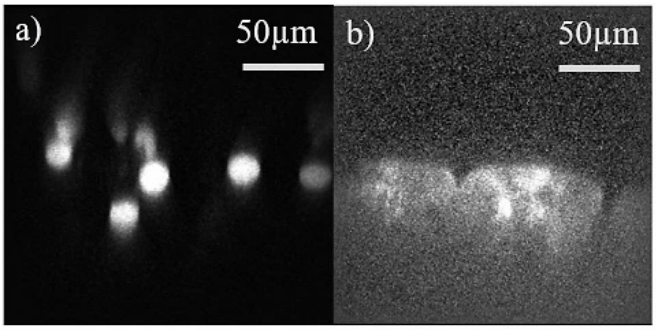

Fig. 16. (a) 15um-diameter bead imaging with 114 Hz $1.6V_{pp}$ $0.8V_{OFF}$ sinusoidal input; (b) FITC dyed mouse colon imaged with 114 Hz $2.8V_{pp}$ $1.4V_{OFF}$ sinusoidal input.

sample was from a tdTomato mouse [28] Tissue was excised from the colon, rinsed with phosphate-buffered saline (PBS), stained with fluorescein, and mounted on a glass slide for imaging. Features of the colon epithelium including surface profile and colon crypts can be distinguished. Imaging was performed using voltages of just 1.6 – 2.8 Vpp, less than the full range-of-motion of the device, given limited thickness of the bead phantom and dye penetration in the sample tissue.

Imaging results indicate that a field of view of at least 300 μm by 300 μm in the x-z plane using the PZT scanner. This exceeds maximum imaging depths achieved in prior endomicroscope prototypes, though at this point being done only on the benchtop setup. Anticipated field-of-view of up to 400 μm when using the scanner over its full range of motion could not yet be verified with available tissue samples. The axial resolution of was approximately 6 μm.

C. Reliability

While full-fledged lifetime testing of the PZT scanners discussed here has not been performed, it is worth addressing several aspects of actuator reliability. First, over the comparatively short term, operation in open-loop leaves potential vulnerability of frequency selection for dynamic balancing to changes in resonant frequency due to changing operating conditions. Fortunately, the low power consumption of the PZT actuators ($< 100\mu$W) minimizes self-heating. Ambient conditions can potentially still contribute to system perturbations, but the required operating conditions for imaging (room temperature to body temperature) are narrow. Repeated tests used to generate frequency response error bars in Fig. 11 indicate reasonable stability of pure z-axis motion over several Hz, though amplitude could vary. After installation in testbed fixtures for imaging, it was sometimes found that a one-time 0.5-1.0 Hz adjustment to input frequency was useful to improve image quality, possibly due to additional stresses generated in the assembly process. We believe that this would be representative of the level of frequency variation that might be expected in typical use.

Over longer durations, thin-film PZT can be expected to age or fatigue. The maximum duration of testing for an actuator similar to the type used for imaging is 40 hours of intermittent use at 10 Vpp and 100 Hz, with no significant change in

performance observed. Previous works on lifetime testing of similar PZT thin-films at comparable or higher voltages have found piezoelectric coefficients to degrade on the order of 10% over $10^8 - 10^9$ cycles [29], [30], which would correspond to almost 2000 hours of use at the tested operating frequency.

Another potential source of concern is the effect of the high laser intensity of a femtosecond laser for multi-photon excitation on the micro-mirror surface. While no damage was observed to the PZT scanner at the tested laser power of 20 mW, tests with static mirrors at 50 mW have showed mirror damage, which places limitations on the maximum power that can feasibly be axially-scanned by a MEMS mirror in the current remote scanning architecture.

VI. Discussion and Conclusions

Multi-photon microscopy is performed for the first time using a thin-film piezoelectric microactuator for fast axial scanning in vertical cross-sectional image acquisition. Actuators achieve large displacements (nearly 200 μm) at low voltages ($< 5V_{\text{pp}}$) near resonance, with the option of frequency selection to isolate pure z-axis translation from rotational components of motion about other axes, even when using a single actuation signal and in the presence of substantial fabrication non-idealities. Analysis of dynamic coupling between modes indicate that such performance can be guaranteed up to various levels of actuator asymmetry or perturbation depending on relative spacing of dominant coupled translation and tilt resonances and on the relative strength of translational versus rotational forcing from individual legs. Fabrication and assembly processes are also refined from previous thin-film piezoelectric microactuator technologies to better support integration into small optical imaging instruments.

Limitations of existing actuator design are minimal optimization of the scanning mirror surface, need to operate and assemble actuators with individual calibration of operating frequency for any static tilt compensation, and potential vulnerability to external vibrations. Future work will examine design optimization to further reduce actuator sensitivity to processing variation and implementation of feedback control systems using embedded sensing elements or optical image features or both to compensate for disturbances and changes in actuator behavior over time.

Appendix A

This appendix reviews PZT scanner leg static deformation modeling previously introduced in [7] and [8], and summarizes other model parameters used in modeling.

Leg stiffness is computed under Bernoulli beam bending assumptions for the serpentine beam structure shown in Fig. 17, having segments with two distinct composite moduli. The initial segment of each fold in the leg has a smaller modulus and bend upward under an applied piezoelectric force, while the latter segment has a larger modulus due to an additional aluminum layer, which results in downward bending under piezoelectric forcing.

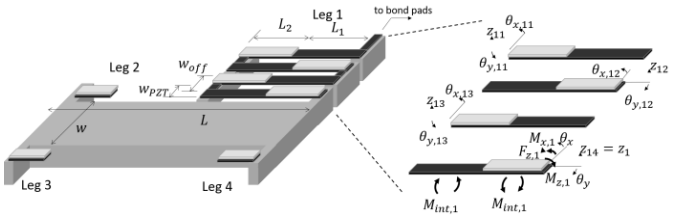

Fig. 17. Schematic layout of mirror platform and first serpentine leg, with exploded leg schematic to define individual element tip displacement variables and reaction forces at connection to mirror platform.

A compliance matrix, $\mathbf{C}_i$, can be generated for a nominal leg structure by calculating the displacement in various axes due to a force or moment at the leg tip. For example, response of the leg in Fig. 1 to a force, F_z, in the z-direction at its tip is a summation of the F_z's contribution to bending in each link as well as torsion of beams 1-3 due to lateral separation of each beam by distance W. This is generated by sequential computation of effects of an external force on displacements along the serpentine leg, i.e.:

$$z_{11} = \frac{L_1^3 F_{z1}}{3\,(EI)_1} + \frac{L_2^3 F_{z1}}{3\,(EI)_2} - \frac{L_1^2 F_{z1}\,(L_1+L_2)}{2\,(EI)_1} - \frac{L_2^2 F_{z2}\,(L_1+L_2)}{2\,(EI)_2} + \frac{L_1 L_2^2 F_{z1}}{2\,(EI)_2} + \frac{L_1 L_2 F_{z1}\,(L_1+L_2)}{(EI)_2} \tag{11}$$

$$\theta_{y,11} = \frac{L_1^2 F_{z1}}{2\,(EI)_1} + \frac{L_2^2 F_{z1}}{2(EI)_2} - \frac{L_1 F_{z1}\,(L_1+L_2)}{(EI)_1} - \frac{L_2 F_{z1}\,(L_1+L_2)}{(EI)_2} \tag{12}$$

$$\theta_{x,11} = -\frac{L_1 F_{z1}(3w_{off})}{(GI_{xx})_1} - \frac{L_1 F_{z1}(3w_{off})}{(GI_{xx})_1} \tag{13}$$

and adding additional compliance sequentially, where z_{ij}, $\theta_{y,ij}$, and $\theta_{z,ij}$ are the vertical displacement, out-of-plane bending rotation, and torsional rotation of the tip of beam j in leg i,$(EI)_1$ and $(EI)_2$ are the composite bending moduli and $(GI_{xx})_1$ and $(GI_{xx})_2$ are composite torsion moduli of the multi-layer material stacks in the bend-up and bend-down portions of each leg, w_{off} is the offset between parallel beams in the leg, and L_1 and L_2 are the lengths of the respective segments. Complete compilation of compliance behavior for this leg architecture has been presented in [8]. The resulting nominal stiffness matrix, $\mathbf{K}_i = \mathbf{C}_i^{-1}$ for individual serpentine legs mirror design in this paper was calculated as:

for displacement vector $\mathbf{x}_i = [z_i \theta_{yi} \theta_{xi}]^T$.

$$\mathbf{K}_i = \begin{bmatrix} 0.023\text{N/m} & -1.6\times10^{-8}\text{N/rad} & -9.6\times10^{-6}\text{N/rad} \\ -1.6\times10^{-8}\text{Nm/m} & 2.6\times10^{-8}\text{Nm/rad} & -6.7\times10^{-9}\text{Nm/rad} \\ 9.6\times10^{-6}\text{Nm/m} & -6.7\times10^{-9}\text{Nm/rad} & 5.1\times10^{-9}\text{Nm/rad} \end{bmatrix} \tag{14}$$

The bending moment generated in each segment of the legs by the PZT film, M_{int}, can be calculated from

$$M_{int,i} = d_{31,eff} V w_{PZT} E_{PZT} (\bar{y}_{PZT} - \bar{y}_i) \tag{15}$$

where $d_{31,eff}$ is an effective piezoelectric strain coefficient, w_{PZT} is the width of the PZT layer, E_{PZT} is the nominal elastic modulus of the PZT layer, $\bar{y}_{PZT}$ is the midline of the PZT film, and $\bar{y}_i$ is the neutral axis of the PZT stack for $i = 1$ or 2 representing the 'up' or 'down' bending segment being considered. This results in a net translation and rotation at the i-th leg tip, were it moving freely in space with perfectly identical beam dimensions and properties of:

$$z_i = 4\left(\frac{M_{int,1}L_1^2}{2(EI)_1} - \frac{M_{int,2}L_1^2}{2(EI)_2}\right) \tag{16}$$

$$\theta_{y,i} = \pm 4\left(\frac{M_{int,1}L_1}{2(EI)_1} + \frac{M_{int,2}L_2}{2(EI)_2}\right) \tag{17}$$

where the sign of the second term depends on the leg being considered, and $M_{int,1} > 0$ while $M_{int,2} < 0$ giving large free translation with limited tip rotation in the bend-up/bend-down configuration. Total rotation θ_y of the mirror is nominally zero across the summation of forces from all legs. Similarly, there is zero nominal rotation of the leg tip about the x-axis, though in this case due to a lack of piezoelectric forcing in that direction for the individual legs

The forces and moments at the end of the leg, $\mathbf{F}_i = [F_{z,i}\ M_{x,i}\ M_{y,i}]^T$, contribute to forces and moments about the mirror platform center of gravity, $\mathbf{F}$, based on moment arm matrices, $\mathbf{T}_i$,

$$\mathbf{F} = \sum_{\mathbf{i=1}}^{\mathbf{4}} \mathbf{T}_i \mathbf{K}_i \mathbf{x}_i \tag{18}$$

where for example $\mathbf{T}_1$ is given by

$$\mathbf{T}_1 = \begin{bmatrix} -1 & 0 & 0 \\ -w/2 & -1 & 0 \\ -L/2 & 0 & -1 \end{bmatrix} \tag{19}$$

with $L$the mirror platform length and w its width. Similarly, for small angle rotations, displacement at the tip of the legs are related to central mirror platform displacement by matrices $\mathbf{S}_i$, i.e. for leg 1,

$$\mathbf{x_1} = \mathbf{S}_1\mathbf{x} = \begin{bmatrix} -1 & w/2 & -L/2 \\ 0 & -1 & 0 \\ 0 & 0 & -1 \end{bmatrix} \mathbf{x}. \tag{20}$$

The above models are then used to create the stiffness and input matrices used in analysis of PZT scanner dynamics.

ACKNOWLEDGMENT

The authors thank the staff at the Lurie Nanofabrication Facility at the University of Michigan and Radiant Technologies for their assistant in device fabrication.

REFERENCES

[1] D. M. Huland, K. Charan, D. G. Ouzounov, J. S. Jones, and C. Xu, "Three-photon excited fluorescence imaging of unstained tissue using a GRIN lens endoscope," *Biomed. Opt. Exp.*, vol. 4, no. 5, pp. 652–658, 2013.

[2] Y. Wu, Y. Leng, J. Xi, and X. Li, "Scanning all-fiber-optic endomicroscopy system for 3D nonlinear optical imaging of biological tissues," *Opt. Exp.*, vol. 17, no. 10, pp. 7907–7915, 2009.

[3] C. L. Hoy *et al.*, "Miniaturized probe for femtosecond laser microsurgery and two-photon imaging," *Opt. Exp.*, vol. 16, no. 13, pp. 9996–10005, 2008.

[4] D. R. Rivera, C. M. Brown, D. G. Ouzounov, W. W. Webb, and C. Xu, "Multifocal multiphoton endoscope," *Opt. Lett.*, vol. 37, no. 8, pp. 1349–1351, 2012.

[5] D. G. Ouzounov *et al.*, "Dual modality endomicroscope with optical zoom capability," *Biomed. Opt. Exp.*, vol. 4, no. 9, pp. 1494–1503, 2013.

[6] H. Bao, J. Allen, R. Pattie, R. Vance, and M. Gu, "Fast handheld two-photon fluorescence microendoscope with a 475 μm × 475 μm field of view for *in vivo* imaging," *Opt. Lett.*, vol. 33, no. 12, pp. 1333–1335, 2008.

[7] Z. Qiu *et al.*, "Large displacement vertical translational actuator based on piezoelectric thin films," *J. Micromech. Microeng.*, vol. 20, no. 7, p. 075016, 2010.

[8] J. Choi, C.-H. Rhee, T. D. Wang, and K. R. Oldham, "A three-degree-of-freedom thin-film PZT-actuated microactuator with large out-of-plane displacement," *J. Micromech. Microeng.*, vol. 24, p. 075017, Sep. 2014.

[9] Y. Zhu, W. Liu, K. Jia, W. Liao, and H. Xie, "A piezoelectric unimorph actuator based tip-tilt-piston micromirror with high fill factor and small tilt and lateral shift," *Sens. Actuators A, Phys.*, vol. 167, no. 2, pp. 495–501, 2011.

[10] J. F. Domke, C.-H. Rhee, Z. Liu, T. D. Wang, and K. R. Oldham, "Amplifying transmission and compact suspension for a low-profile, large displacement piezoelectric actuator," *J. Micromech. Microeng.*, vol. 21, no. 6, p. 067004, 2011.

[11] E. E. Aktakka, R. L. Peterson, and K. Najafi, "A 3-DOF piezoelectric micro vibratory stage based on bulk-PZT/silicon crab-leg suspensions," in *Proc. IEEE Int. Conf. Microelectromech. Syst.*, Taipei, Taiwan, Jan. 2013, pp. 576–579.

[12] X. Zhang, C. Duan, L. Liu, X. Li, and H. Xie, "A non-resonant fiber scanner based on an electrothermally-actuated MEMS stage," *Sens. Actuators A, Phys.*, vol. 233, pp. 239–245, Sep. 2015.

[13] C.-P.-B. Siu, H. Zeng, and M. Chiao, "Magnetically actuated MEMS microlens scanner for *in vivo* medical imaging," *Opt. Exp.*, vol. 15, no. 18, pp. 11154–11162, 2007.

[14] H. Li *et al.*, "Integrated monolithic 3D MEMS scanner for switchable real time vertical/horizontal cross-sectional imaging," *Opt. Exp.*, vol. 24, no. 3, pp. 2145–2155, 2016.

[15] T. Sandner, T. Grasshoff, and H. Schenk, "Translatory MEMS actuator with extraordinary large stroke for optical path length modulation," in *Proc. IEEE Int. Conf. Opt. MEMS Nanophoton.*, Sapporo, Japan, Aug. 2010, pp. 25–26.

[16] E. J. Botcherby *et al.*, "Aberration-free three-dimensional multiphoton imaging of neuronal activity at kHz rates," *Proc. Nat. Acad. Sci. USA*, vol. 109, no. 8, pp. 2919–2924, 2012.

[17] X. Duan, H. Li, X. Li, K. Oldham, and T. Wang, "Remote axial scanning with MEMS-based multiphoton microscopy," *Opt. Exp.*, vol. 25, no. 3, pp. 2195–2205, Feb. 2017.

[18] J. Felder, E. Lee, and D. DeVoe, "Large vertical displacement electrostatic zipper microstage actuators," *J. Electromech. Syst.*, vol. 24, no. 4, pp. 896–903, 2015.

[19] K. Murari, Y. Zhang, S. Li, Y. Chen, M.-J. Li, and X. Li, "Compensation-free, all-fiber-optic, two-photon endomicroscopy at 1.55 μm," *Opt. Lett.*, vol. 36, no. 7, pp. 1299–1301, 2011.

[20] H. Bao, A. Boussioutas, J. Reynolds, S. Russell, and M. Gu, "Imaging of goblet cells as a marker for intestinal metaplasia of the stomach by one-photon and two-photon fluorescence endomicroscopy," *J. Biomed. Opt.*, vol. 14, no. 6, p. 064031, 2009.

[21] C. Wang and N. Ji, "Characterization and improvement of three-dimensional imaging performance of GRIN-lens-based two-photon fluorescence endomicroscopes with adaptive optics," *Opt. Exp.*, vol. 21, no. 22, pp. 27142–27154, 2013.

[22] A. Straub, M. E. Durst, and C. Xu, "High speed multiphoton axial scanning through an optical fiber in a remotely scanned temporal focusing setup," *Biomed. Opt. Exp.*, vol. 2, no. 1, pp. 80–88, 2010.

[23] X. Duan *et al.*, "MEMS-based multiphoton endomicroscope for repetitive imaging of mouse colon," *Biomed. Opt. Exp.*, vol. 6, no. 8, pp. 3078–3083, 2015.

[24] N. Safdarian *et al.*, "Quantifying human eosinophils using 3-dimensional volumetric images collected with multi-photon fluorescence microscopy," *Gastroenterology*, vol. 142, no. 1, pp. 15–20, 2011.

[25] K. Oldham, X. Lin, Z. Qiu, T. Wang, J. S. Pulskamp, and R. G. Polcawich, "Dynamics, sensing, and control of a thin-film piezoelectric vertical micro-stage," in *Proc. ASME Dyn. Syst. Control Conf.*, Cambridge, MA, USA, 2010, pp. 111–118.
[26] Radiant Technologies Inc. *PNZT Coated Wavers With Platinum Bottom Electrodes*, accessed on Mar. 1, 2017. [Online]. Available: http//:www.ferrodevices.com
[27] J. Evans. (2011). *PZT-Silicon Cantilever Benders*. [Online]. Available: http//:www.ferrodevices.com
[28] T. Abe and T. Fujimori, "Reporter mouse lines for fluorescence imaging," *Develop. Growth, Differentiation*, vol. 55, no. 4, pp. 390–405, 2013.
[29] I. Demir, A. L. Olson, J. L. Skinner, R. F. Richards, C.D. Richards, and D. F. Bahr, "High strain behavior of composite thin film piezoelectric membranes," *Microelectron. Eng.*, vol. 75, no. 1, pp. 12–14, 2004.
[30] R. G. Polcawich and S. Trolier-McKinstry, "Piezoelectric and dielectric reliability of lead zrconate titanate thin films," *Lett. Mater. Res.*, vol. 15, no. 11, pp. 2505–2613, 2000.

Jongsoo Choi received the B.S., M.S., and Ph.D. degrees in mechanical engineering from the University of Michigan, Ann Arbor, in 2010, 2011, and 2017, respectively. He is currently with Vesper Technologies Inc., Boston, MA, USA. His research interests include the design, modeling, and fabrication of micro-scale sensors and actuators.

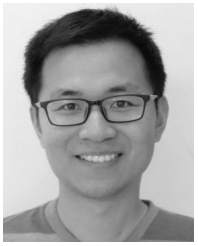

Xiyu Duan received the B.S. degree in electrical engineering from the Hong Kong University of Science and Technology, in 2010, and the Ph.D. degree in biomedical engineering from the University of Michigan, in 2016. He is currently a Post-Doctoral Research Fellow with the Department of Internal Medicine, University of Michigan. His research has focused on MEMS-based fiber endomicroscopes for real time optical biopsy.

Haijun Li received the Ph.D. degree in microelectronics and solid-state electronics from Jilin University, Changchun, China, in 2007. He held a post-doctoral position at Nanyang Technology University, Singapore, from 2008 to 2011. He was a Senior Engineer at the Hebei Semiconductor Research Institute, Shijiazhuang, China, from 1997 to 2008. He is currently a Research Investigator with the University of Michigan, Ann Arbor, MI, USA, where he is involved in the development of MEMS-based endomicroscope. His research interests include MEMS, uncooled infrared detectors, epi-MEMS technology, and wafer level packaging technologies.

Thomas D. Wang received the Ph.D. degree in medical engineering from MIT. He has developed a number of novel optical designs for real time *in vivo* imaging systems. He is currently a Professor of Internal Medicine, Biomedical Engineering, and Mechanical Engineering, and the H. Marvin Pollard Collegiate Professor of Endoscopy Research with the University of Michigan. He is a Senior Member of the Society of Photo-Optical Instrumentation Engineers.

Kenn R. Oldham received the B.S. degree in mechanical engineering from Carnegie Mellon University, in 2000, and the Ph.D. degree in mechanical engineering from the University of California at Berkeley, in 2006. He is currently an Associate Professor of mechanical engineering with the University of Michigan. His research focuses on the intersection of control systems and micro-scale sensing and actuation, with interests in design for controllability, optimal and robust control, microsystem estimation and identification, and novel sensor and actuator design. Applications include terrestrial micro-robotics, endoscopic microscopy, and inertial and physiological sensing.